

DESIGN CONSIDERATIONS AND INITIAL PERFORMANCE OF A 1.2 cm² BETA IMAGING INTRA-OPERATIVE PROBE

Martin P. Tornai, Lawrence R. MacDonald*, Craig S. Levin, Stefan Siegel, Edward J. Hoffman

*Division of Nuclear Medicine & Biophysics, Department of Molecular and Medical Pharmacology,
UCLA School of Medicine, Los Angeles, CA 90095*

**Department of Physics, UCLA, Los Angeles, CA 90095*

ABSTRACT

A novel small area beta (β^\pm) detector is under development for nuclear emission imaging of surgically exposed, radiolabeled tumor beds. The imaging device front-end consists of a 0.5 mm thick by 1.25 cm diameter $\text{CaF}_2(\text{Eu})$ scintillator disk coupled to a rigid bundle of 2 mm diameter double clad optical fibers through a polystyrene light diffuser. The detector area (1.2 cm²) was determined by the requirement of introducing the probe into small cavities, e.g. during neuro-surgical lesion resection, but large enough to produce images of clinical significance. Flexible back-end optical fibers (1.9 m long) were coupled to the front-end components allowing ~ 75 photoelectrons to be detected for mean beta energies of 250 keV, indicating that sufficient signal can be obtained with clinical beta emitters (e.g. ¹⁸F, ¹³¹I). The long flexible fibers guide the scintillation light to a Philips XP1700 series, fiber optic faceplate, Multi-Channel PMT. The parallel MC-PMT outputs are fed into a variable gain, charge divider network and an *i*-V pre-amplifier/line driver network, whose resulting four outputs are digitized and histogrammed with standard Anger positioning logic. The various components in the imaging chain were evaluated and optimized by both simulations and measurements. Line spread functions measured in the 10.8 mm FOV were $0.50 \text{ mm} \pm 0.038 \text{ mm}$ and $0.55 \text{ mm} \pm 0.065 \text{ mm}$ FWHM in X and Y, respectively. A 20% variation in pulse height and minimal variation in spatial resolution was observed. The differential image uniformity was measured to be $\pm 15.6\%$ with ~ 150 cts/pixel. Preliminary images show excellent reproduction of phantom activity distributions.

I. BACKGROUND

Non-imaging radiation detector guided surgery is gaining acceptance for use during clinical tumor resection procedures [1]. In general, there have been fewer advances in non-imaging charged particle detection for tumor localization [2-7] than for non-imaging gamma detection [8-14], partly due to the predominance of gamma emitting radiolabels. As new radiopharmaceuticals are developed for Nuclear Medicine oncological imaging procedures [15,16], intra-operative gamma cameras are being developed to exploit their use during surgery [14,17]. Gamma detection and imaging of subclinical residual radiolabeled tumor deposits can, however, easily be corrupted by concentrations of radioactivity in neighboring tissues, even with low energy gammas. Moreover, real-time, *in situ* emission imaging of charged particles in medicine is not a standard technique and has been restricted to *in vitro* autoradiographic applications [18]. A novel small area beta (β^\pm) detector, which overcomes many of the problems associated with gamma imaging, is under development in our laboratory (Fig. 1) for nuclear emission imaging of intra-operatively exposed, radiolabeled tumor beds [19-23].

The beta imaging probe is intended to delineate the boundaries of radiolabeled tumors, after the bulk of the lesion has been removed. Direct detection of short ranged β^\pm particles facilitates the mapping of radioactive distributions on labeled tissue surfaces and would aid a surgeon in residual lesion identification for removal while sparing unaffected tissues. The technique exploits: (1) the inherent short range of β^\pm particles in tissue; (2) direct source contact eliminating the

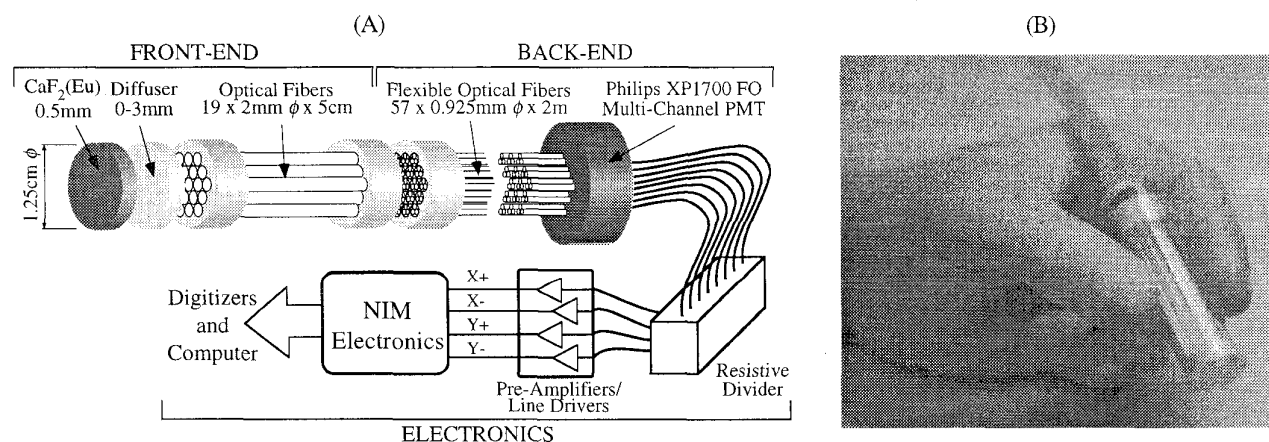


FIGURE 1. (A) Schematic diagram of the beta imaging intra-operative probe. The front-end components are intended to be glued together, and as a unit are removable, sterilizable and exchangeable for other application dependent front-end geometries. Discrete scintillators can be substituted for the continuous disk scintillator as desired. The flexible back-end components and electronics are designed to be universally adaptable to various front-end components. (B) Scale photograph of the actual device described in this paper.

need for a collimator; and (3) detector to source proximity, which has the dual advantage of increased sensitivity [12] and improved resolution [24-28] in nuclear emission imaging.

II. FRONT-END OPTIMIZATION

The front-end of the imaging probe (Fig. 1A) consists of (A) a scintillator with thin ambient light shield (not shown) which comes into direct contact with the tissue surface; (B) a light diffuser to optimize the distribution of the scintillation light; and (C) optical fibers held in a rigid frame.

A. Light Sharing Scintillation Detector

A continuous disk of $\text{CaF}_2(\text{Eu})$ scintillator (Scionix) was optimized for <1 MeV β^\pm particles [22], as use of the device is anticipated with ^{18}F ($E_{\beta^+ \text{ max}} = 635$ keV) and ^{131}I ($E_{\beta \text{ max}} = 606$ keV) labeled pharmaceuticals. $\text{CaF}_2(\text{Eu})$ has a low refraction index (Table 1) which assists in efficient light transfer into optical fibers. The slow decay time is not anticipated to be a problem as low *in vivo* count rates (~ 100 cps) are expected. A 0.5 mm thick by 1.25 cm diameter (ϕ) geometry $\text{CaF}_2(\text{Eu})$ crystal was found to have optimal properties in terms of light output, and minimal contribution from background (e.g. from 511 keV gammas if β^+ s are used) [22].

TABLE 1. Comparison of detector candidates and NaI(Tl).

PROPERTY	SCINTILLATOR		
	NaI(Tl)	BC404	$\text{CaF}_2(\text{Eu})$
Light Output (ph/MeV)	38k	11.2k	24k
Max Emission λ (nm)	415	423	435
Density (g/cm ³)	3.67	1.03	3.19
Decay Constant (nsec)	230	2.4	940
Refractive Index (n)	1.85	1.58	1.44
Bulk Attenuation (cm)	~ 40	160	~ 2.5

Since the imaging device will be used in surgery, ambient light must be shielded with an opaque reflector. Optical photon tracking Monte Carlo simulations with DETECT [29] aided in determining optimum surface treatments on the front face of the cylindrical detector. To eliminate the high reflections from the edge, which can cause mispositioning errors [27], absorbing sides were simulated on all cylindrical scintillator configurations. For various surface treatments, the simulation results showed a decrease in light spread (Fig. 2) and an increase in light output for thinner scintillators [22,23]. These trends imply both better photon statistics for positioning, and the ability to control further light spread with thinner scintillators. For simulated isotropically emitting light sources, the light spread was non-Gaussian, hence the root mean squared deviation (RMSD) was calculated. Simulated photon emission at various depths had little effect on light spread in thin (<1.5 mm) crystals.

All further measurements and simulations were performed with a 0.5 mm thick by 1.25 cm ϕ $\text{CaF}_2(\text{Eu})$ scintillator with roughened upper surface (near beta sources) and a thin Teflon layer covering the crystal. This optimum (thin) front-end reflector determined from the simulations was confirmed with measurements [22].

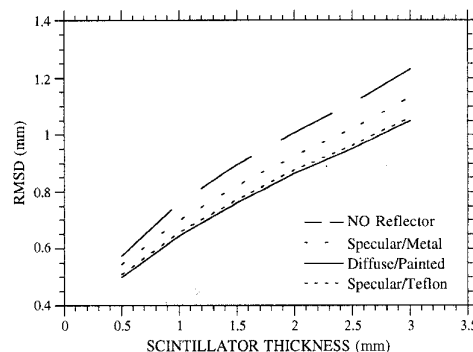


FIGURE 2. Simulated RMSD light spread at the center of a 1.25 cm ϕ and various thickness scintillators optically coupled to a position sensitive, glass faceplate PMT. With decreasing scintillator thickness, light output increased. The key describes crystal surface condition and type of reflector.

B. Diffusing Light Guide

The light diffuser (Fig. 1A) is an important component that controls scintillation light spread among the front-end fiber optic elements. The type and geometry of light diffuser affects both the light transmission from the scintillator into the front-end fibers, and also the spatial resolution of the device. Too great a spread of light decreases the precision of position estimation [30,31]; too small a spread makes it difficult to interpolate between front-end fiber elements ([20] and Fig. 14A).

The optical light diffusers investigated were made of (1) quartz ($n=1.46$), (2) clear polymethylmethacrylate (PMMA, $n=1.49$), (3) glass ($n=1.50$), and (4) polystyrene (PS, $n=1.58$) (the same material as the core of the Kuraray double clad polystyrene core (DCPS) optical fiber; see section II.C. for fiber optimization). Transmission measurements were made on ~ 2.25 mm thick by 1.25 cm ϕ , highly polished light diffuser samples with a Beckman UV Spectrophotometer (DU640) with an integrated photodiode detector (Fig. 3). There was a 6% variation in transmission at 435 nm ($\text{CaF}_2(\text{Eu})$ emission peak) between glass and PS. The greatest differences between samples were at the cutoff wavelengths, all of which were well below the peak emission λ of $\text{CaF}_2(\text{Eu})$.

Pulse height measurements were also made with the thin $\text{CaF}_2(\text{Eu})$ scintillator coupled through various thicknesses of PS and PMMA light guides (0.5 - 3.0 mm) to a front-end bundle of 19, 2 mm ϕ DCPS fibers in a white PMMA holder

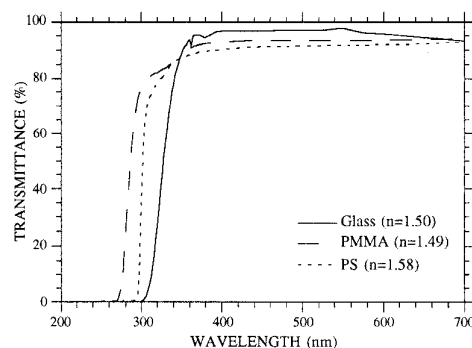


FIGURE 3. Measured transmittance for glass (2.3 mm), clear PMMA (2.25 mm), and clear PS (2.25 mm).

(Fig. 1), and irradiated with ^{204}Tl ($\beta^- E_{\beta \text{ max}} = 763 \text{ keV}$) (Fig. 4). Simulations of the measurement set-up indicated that given the same bulk attenuation properties and only refractive index differences for the two light diffusers, there was a slight light transmission improvement (4%) for PS versus PMMA light guides. The $\sim 10\%$ measured pulse height difference between the PS and PMMA light guides (Fig. 4) is then a combination of the bulk transmission and refractive index variations of the materials.

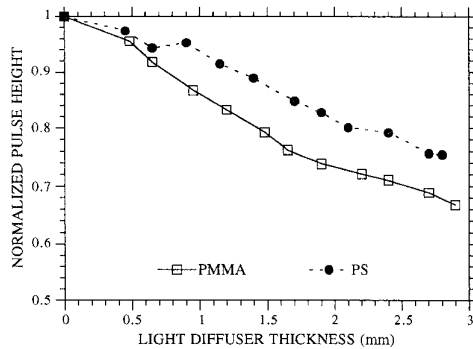


FIGURE 4. Measured pulse height from ^{204}Tl irradiated 0.5 mm thick $\text{CaF}_2(\text{Eu})$ disk, covered with 1 layer of Teflon, through PMMA and PS light guides coupled via bundle of 19, 2 mm ϕ by 10 cm long DCPS fibers to MC-PMT. Coupling grease ($n=1.49$) was the near optimum for all interfaces.

The light spread function (LTSF = pulse height vs. position) was simulated for a 0.5 mm by 1.25 cm ϕ $\text{CaF}_2(\text{Eu})$ scintillator optimally coupled to either PMMA/glass ($n_{\text{PMMA}} \approx n_{\text{glass}}$), PS, or quartz light diffusers with a 2 mm ϕ DCPS fiber at the center (Fig. 5A). The light diffusers were varied in thickness, and were connected at the scintillator end to either a white, black, or aluminum fiber holder (reflective support structure; see section II.D.). The profiles of the LTSFs (Fig. 5B and 5C) were roughly Gaussian but varied in the amplitude of the tails: higher tails for the more reflective white fiber holder, lower tails for the Al and black holders (Fig. 8). The LTSF FWHMs for different diffuser materials varied only slightly indicating that the reflective properties of the holders played a larger role in the light spread than the refractive indices of the light guides. The shape of the LTSF may be a result of the convolution among the intrinsic Poisson light distribution, Lambertian (cosine distributed) reflections from diffuse surfaces, and a function which accounts for the fixed acceptance angle (NA) of the optical fiber.

Although the best transfer efficiency and also the narrowest light spread from scintillator to fiber optic occurs when there is no light diffuser, the device's imaging ability will depend on light sharing between the fiber optic elements [20,21]. There is a trade-off, then, between light collection and optimum light spread which will affect the spatial resolution and energy response (see section V.A.).

C. Front-End Fiber Optics

The best type of front-end optical fiber was determined from the measured transmission properties of eight 2 mm ϕ fibers with various numerical apertures ($\text{NA} = 0.4 - 0.72$) and core materials (PS, PMMA, glass, quartz). The 2 mm ϕ of the optical fiber was initially determined by MCNP Monte

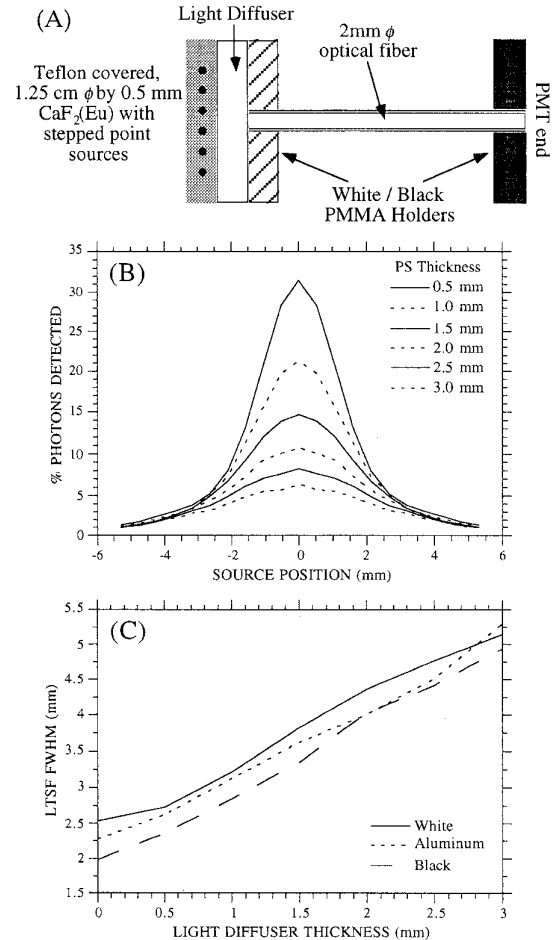


FIGURE 5. (A) Simulation set-up for the LTSF measurement with various light diffusers. Scintillator had diffuse upper reflecting surface and diffuse absorbing sides. (B) Variation of the simulated LTSF for $\text{CaF}_2(\text{Eu})$ on various thickness PS light guides connected to white reflective fiber holder with 2 mm ϕ by 15 cm long DCPS optical fiber. The integral of these curves indicates the total light collected by a single fiber. (C) Variation of LTSF FWHM for simulated PS light guides and different reflectivity fiber holders.

Carlo simulations of optimal electron energy deposition requirements from $\sim 700 \text{ keV}$ electrons in plastic scintillators for use in discrete versions of the imaging probe (e.g. in [19,22]).

Fibers, 30 cm long, were attached with optical grease ($n = 1.49$) to the $\text{CaF}_2(\text{Eu})$ scintillator (covered with a layer of Teflon) through a white PMMA fiber holder and also through a hole on a black faceplate on an RCA C31024 PMT (see Fig. 5A). The PMT gain was calibrated with single photoelectron (PE) measurements [32]. The measured pulse height with ^{204}Tl beta irradiation was calculated as the weighted mean of the beta distribution, which was shown to be a reliable indicator of the mean light output from thin scintillators [23].

The LTSF was measured for all the optical fibers with the scintillator attached, and the integrated LTSF distribution ("mean total") yielded the total light detected through the fiber (Fig. 6). As the NA increased, the total number of detected PEs also increased, which is consistent with the greater

acceptance angle (NA) of the fiber. An inverse relationship was found between the measured LTSF FWHM and increasing fiber NA, which is counter intuitive. However, the LTSF FWHM decreased with increasing PE statistics (Fig. 7), indicating that fiber NA, hence light collection, had a greater effect for photon emissions originating directly over the center of the fiber than at some distance away.

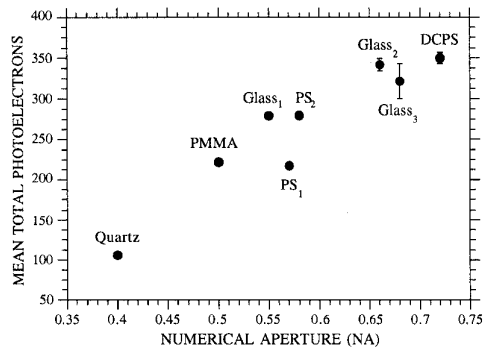


FIGURE 6. Measured number of PEs from the integrated LTSF for various core material, 2 mm ϕ optical fibers. Values are normalized for fiber area. PMMA = polymethylmethacrylate, PS = polystyrene, DCPS = double clad PS. Subscripts indicate different material compositions.

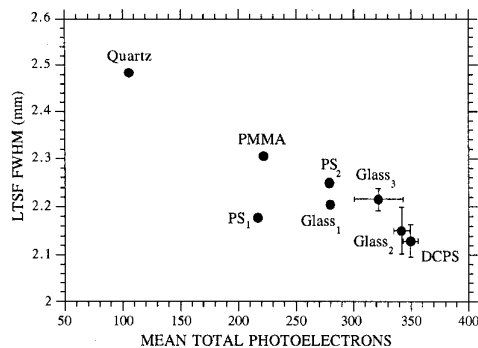


FIGURE 7. LTSF FWHM as a function of increasing PE statistics for various core material and NA, 2 mm ϕ optical fibers with $\text{CaF}_2(\text{Eu})$. Error bars are for multiple measurements.

The DCPS plastic optical fiber (Kuraray Int'l) was determined to have the best properties, both in terms of light transmission for $\text{CaF}_2(\text{Eu})$ light, and material composition. The DCPS fiber is a multi-mode, step index, double clad PS core fiber ($n_{\text{core}} = 1.59$, $n_{\text{inner clad}} = 1.49$, $n_{\text{outer clad}} = 1.42$). In general, the transmission in optical fibers is affected by the cladding condition [33], e.g. surface roughness. The outer fluorinated polymer cladding in the DCPS optical fibers ensures an excellent first cladding interface, relatively free of imperfections [19,34].

D. Detector & Fiber Structural Support

The input fibers are held in a close packed hexagonal arrangement of 19 fibers maximizing surface coverage (Fig. 1). This is a standard, close packed arrangement similar to that used for PMTs in Nuclear Medicine gamma cameras [24-28]. The 2 mm ϕ fibers are spaced on 2.2 mm centers to allow enough material to hold the fibers in place without optical crosstalk. Four holders, 5 mm thick by 1.25 cm ϕ

with 2 mm ϕ holes, were tested: PMMA (all white, all black, and 1:4 mm black:white mixture), and aluminum. 5 cm long DCPS optical fibers were glued into each holder and polished. These holders are removable from the back-end fiber optics (Fig. 1) and are intended to be exchangeable with various geometry front-ends developed for specialized surface imaging applications.

The light spread function was first measured for 10 cm long single fibers centered in holders described above, and compared with simulations (Fig. 8). There was an excellent correlation between the measurements and simulations. The largest variations occurred with the Al holder. Note that there were lower tails and a lower total pulse height with the more absorbing support structures, consistent with other measurements [31].

The light output of the assembled front-end (19 fibers) was measured with ^{204}Tl irradiation of the 0.5 mm $\text{CaF}_2(\text{Eu})$ scintillator covered with Teflon and coupled with optical grease to the various front-end DCPS fiber bundle holders and in turn coupled to a single channel PMT (single PE calibrated C31024) (Table 2). In addition, a front-end fiber bundle made with PS core single clad fibers (Bicron BCF98, NA = 0.58) was made for comparison. A 1.08 mm \pm 0.09 mm spatial resolution with a pre-prototype imaging device was measured with the NA = 0.58 BCF98 fibers [20]. With the present holder light output results (Table 2), we would expect a 20% improvement in spatial resolution in the white holder with

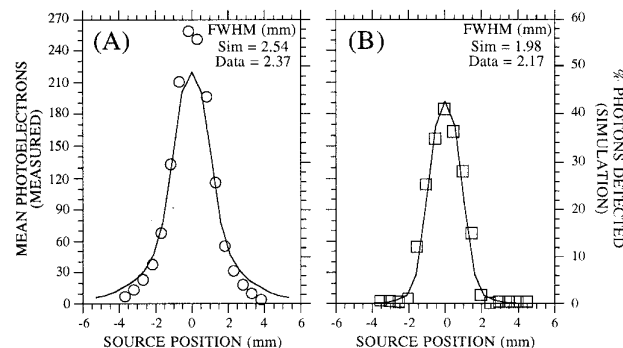


FIGURE 8. DCPS fiber in a white (A) and black (B) holder coupled to the scintillator and covered with Teflon. Note the good correlation between measurements (symbols) and simulations (lines). The integral of each curve corresponds to the total light collected by the single fiber from this light distribution. Note both the lower tails and smaller number of detected photons with the black holder.

TABLE 2. Comparison of light yield with directly coupled $\text{CaF}_2(\text{Eu})$ on different front-end holders and 19 DCPS fibers. Errors shown are for multiple measurements.

Holder Type	Mean Total PEs
White	254.8 \pm 6.7
Black	147.0 \pm 3.9
Black & White (1:4)	152.7 \pm 7.8
Aluminum	133.4 \pm 4.2
White*	160.6 \pm 2.7

*White holder with NA = 0.58 fibers.

DCPS fibers compared to the BCF98 pre-prototype due to light collection (Poisson statistics) alone. Although the light collection with the low reflectivity holders and DCPS fiber was poorer than with the BCF98 fibers, we may expect improved resolution due to the absorbing effect of the inter-fiber holder material [30,31], leading to less positioning error (cf. the tails in Fig. 8, and see section V.B.).

The pulse height with different fiber bundle holders in the optimal imaging device (see section III.B.) was also characterized with a 1.7 mm thick PS diffusing light guide (see section V.A.) between the scintillator and fiber bundle. Normalized to the white holder response, the pulse height variation was $1.0 \pm 0.6\%$, $0.91 \pm 0.3\%$, and $0.74 \pm 0.2\%$ for the white, black and Al holders, respectively. These somewhat smaller pulse height variations may be partly due to (1) better optics with the 1.7 mm thick PS light diffuser between the scintillator and fibers, and (2) that the diffusing light guide optics smoothed out any differences seen in the direct crystal/fiber interface case.

III. BACK-END OPTIMIZATION

The back end consists of: (A) a holder to accurately flange to the front-end and hold (B) longer, more flexible, smaller diameter DCPS fiber bundles that conduct the signal to (C) the photon detector. Other important components include: (D) an optical alignment mask to flange the fibers to the photon detector; (E) the positioning electronics and preamplifiers; and (F) NIM modules for signal amplification, ADCs and a computer for image processing.

A. Fiber Optics

The back-end fiber optics are expected to be ~ 2 m in length [19-21] but could easily and advantageously be made shorter. They need to have long attenuation lengths for the scintillator wavelength(s) of interest, be flexible, and be durable. The optimum back-end fiber was also chosen to be DCPS fiber due to its overall excellent transmission properties with $\text{CaF}_2(\text{Eu})$ ([19,34] and Fig. 6). Alignment masks to hold the back-end fibers are identical to the front-end fiber holders.

B. Bundle Arrangement

For light diffuser and fiber holder optimization measurements in the assembled imaging device, a high resolution device was fabricated from 19, 10 cm long by 2 mm ϕ DCPS fibers (see section V.) coupled directly to the multi-element photodetectors (PD). Measurements for the intended longer flexible fibers, however, were also undertaken to determine the device feasibility in these lower light, yet surgically accommodating conditions.

Three diameters of DCPS optical fibers were tested: 0.835 mm, 0.925 mm, and the reference 2.0 mm ϕ fibers. Tests were conducted by bundling and optically cementing ($n_{\text{glue}} = 1.56$) four 0.835 mm, or three 0.925 mm, or single 2.0 mm ϕ fibers, all 15 cm long, into a white PMMA holder (Fig. 9). The LTSF and total light output were measured (as described in sections II.B. and II.C.) with the 0.5 mm thick $\text{CaF}_2(\text{Eu})$ disk covered with Teflon and optically coupled to a 2 mm ϕ by 5 cm DCPS fiber and white holder flanged to the respective back-end test “bundles” (Table 3). A non-negligible contribution of the signal arises due to cladding transmission of

optical photons in short fibers [33]. The differences seen between the short (15 cm) fiber bundles are less than that expected for longer lengths (190 cm) because of increased multiple reflections in the smaller diameter fibers. Although attenuation lengths may be similar for various diameter (same material) fibers, the total transmission in smaller diameter fibers does not simply decrease by the differences in area, since more internal reflections in smaller diameter fibers lead to greater transmission losses. This effect was corroborated by Monte Carlo simulations.

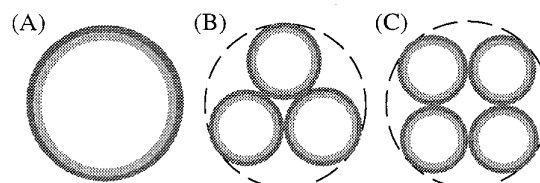


FIGURE 9. Various fiber arrangements for the back-end DCPS fibers inscribed in a 2 mm ϕ holder. (A) 2.0 mm ϕ reference fiber; (B) 3 x 0.925 mm ϕ fibers, and (C) 4 x 0.835 mm ϕ fibers.

TABLE 3. Comparison of light transmissions for ^{204}Tl beta irradiation of $\text{CaF}_2(\text{Eu})$ scintillator through various “bundles” and lengths of back-end fiber optics. Errors shown are for multiple measurements (15 cm) and PE statistics (190 cm).

# Fibers	Diameter (mm)	Area Ratio*	Mean Total PEs ($\pm\sigma$)	
			15 cm	190 cm
1	2	1	288.1 ± 44.5	180.8 ± 13.4
3	0.925	0.642	208.1 ± 2.9	73.3 ± 8.6
4	0.835	0.697	205.3 ± 12.8	-

*Area covered by fiber bundles to the 2 mm ϕ fiber area.

When the integral LTSF was measured with the 1.9 m lengths, larger differences resulted (Table 3). Even though there was a 60% transmission loss in going from the long, inflexible yet optimal 2 mm ϕ back-end fiber to the more flexible, three 0.925 mm ϕ back-end fibers, a large number of PEs were detected at the PMT. Note that the integrated LTSF only accounts for one dimensional light contribution into a given fiber and that a 2D array of fibers may detect more total PEs. On the order of 70 PEs has been shown to be sufficient for use in energy and positioning information [19,20,26,28].

IV. PHOTON DETECTOR & POSITIONING ELECTRONICS

The multi-channel PMT (MC-PMT) package is the proposed PD for this case because of (A) the relatively simple implementation to readout optical fibers, (B) the ability to detect the anticipated signal levels (see Table 3), and (C) the parallel readout of the device. To identify the optimum placement of the back-end fibers on the photon detector elements or pixels, the optical and inherent electronic crosstalk properties of two MC-PMTs were evaluated. The Philips XP1702 and XP1722 [35-38] are 64 channel (8 x 8 pixels, each 2.54 mm on a side) MC-PMTs with bialkali photocathodes, differing only in their optical input windows: the XP1702 has a continuous borosilicate glass faceplate ~ 3

mm thick, and the XP1722 has an ~ 5 mm thick fiber optic (FO) faceplate with $50 \mu\text{m}$ ϕ fibers (NA = 1.0).

A. Optical Faceplate Measurements

The optical transmission properties of two samples of input windows were measured (as described in section II.B.). Note both a higher transmittance and shorter wavelength cutoff for the glass faceplate tube (Fig. 10). This result is not surprising as the transmission through fibers is known to be lower than in bulk material. The cutoff at higher wavelengths (~ 350 nm) for the FO faceplate may be due in part to the $50 \mu\text{m}$ ϕ of the fibers, which attenuates higher frequencies more than lower frequencies (see III.B.) and also the physical properties (e.g. transmission) of the fiber cladding material, which are necessarily different than the core material. This measurement shows one effect of the total light detected at a single element in the MC-PMT.

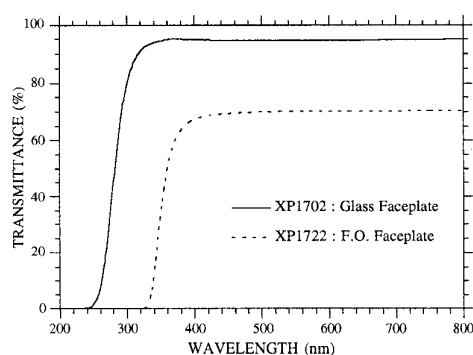


FIGURE 10. Measured transmittance of the front faceplates of two Philips MC-PMTs (faceplates were 3 mm and 5 mm thick for the XP1702 and XP1722, respectively)

B. Point Spread Function

Point spread function measurements were performed on both MC-PMTs pulsed with a green LED (~ 565 nm) through a 50 cm long by 0.835 mm ϕ DCPS fiber (NA = 0.72), a similar type as in the intended components of the back-end flexible fiber bundle. The fiber was embedded in a black PMMA holder and raster scanned with an XYZ-translation stage in 0.5 mm regular increments around the inner 16 pixels of the 8×8 discrete pixel arrays of both MC-PMTs.

1000 events were collected per LED/fiber position. All measurements were pedestal corrected and adjusted for gain variation among pixels (determined from flood field illuminations). It was estimated that >100 PEs were produced at the photocathode of either PMT per LED pulse. The spatial responses of the MC-PMTs had pixel FWHMs of $3.18 \text{ mm} \pm 0.038 \text{ mm}$ and $2.20 \text{ mm} \pm 0.16 \text{ mm}$ for the XP1702 (glass) and XP1722 (FO), respectively (Fig. 11). Note the sharper delineation of the pixel in the FO faceplate MC-PMT which implies lower crosstalk between adjacent horizontal, vertical and diagonal elements.

C. Crosstalk

Crosstalk is defined as the fraction of the total signal that is not collected by the pixel of interest but is collected by the

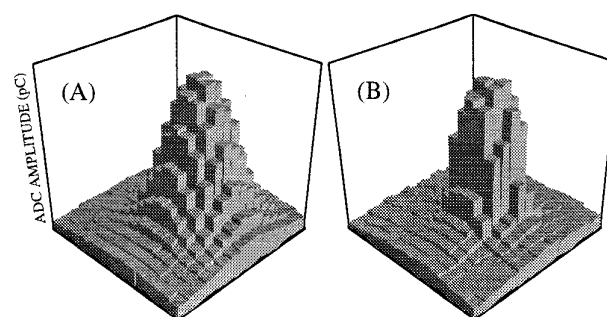


FIGURE 11. 2D PSF histogram of a 2.54 mm square pixel on the XP1702 (A) and XP1722 (B) MC-PMTs. Each amplitude (in the 16×16 histogram) represents the pixel's response to the input LED/fiber at a different location on the inner 16 pixels of the MC-PMT. All blocks are 0.5 mm apart in X and Y.

immediately adjacent (horizontal, vertical and diagonal) pixels. The fraction of collected light for a pixel and crosstalk fraction were measured and then normalized by the transmission properties of the MC-PMT faceplates (at ~ 565 nm) in order to determine the fraction of the total light collected by the pixel-of-interest to the total light coming into the MC-PMT.

The total single pixel signals for back-end fibers in a single bundle-set (i.e. 3 fibers to 1 pixel) were 28.7% and 31.0% ($\pm 5.6\%$ for both MC-PMTs) with a total crosstalk of 66.0% and 39.0% of the total incoming light, for the XP1702 and XP1722, respectively. When the back-end fibers fanned out so that each fiber was coupled to its own pixel element (i.e. 3 fibers to 3 pixels), the total pixel signals were $47.7\% \pm 8.1\%$ and $42.5\% \pm 3.0\%$ and total crosstalk signals were 47.0% and 27.5% of the total incoming light, for the XP1702 and XP1722, respectively.

Note that when the back-end fibers were connected to individual pixels (i.e. 3 fibers to 3 pixels) both the total signal collected in the pixel-of-interest improved by 66% and 37%, for the XP1702 and XP1722, respectively, and that the total crosstalk into adjacent pixels decreased by $\sim 40\%$ for both MC-PMTs. The improvement in crosstalk with combinations of pixels (i.e. 3 pixels each with a fiber vs. 1 pixel with three fibers) is not surprising as the increased distance between pixel elements provides the light a smaller solid angle to travel into the neighboring pixels.

The surprising result obtained was that the XP1722 MC-PMT, including transmission losses in the FO faceplate, had approximately the same total pixel signal as the XP1702. This result indicates that coupling fibers to the FO faceplate MC-PMT gives the same signal intensity at a given pixel with considerably lower crosstalk. Minimal signal crosstalk is very important for processing the discretized (fiber) signals from the front-end light sharing detector, as used in this imaging device.

The intended MC-PMT is the Philips XP1724, which is a 96-channel FO faceplate MC-PMT with similar characteristics as the XP1722 evaluated in this work. With 96 channels there will be considerably more flexibility in fiber/PMT coupling with continued imaging detector evaluation and development.

D. Positioning Readout Electronics

In order to minimize the electronic hardware involved in the imaging chain, a simple charge division readout scheme [20,39,40] was developed and optimized for the imaging probe (Fig. 12). The readout consists of a resistor network with four resistors, whose fixed values correspond to the Cartesian locations [28] of the front-end optical fibers attached to a pixel element from the MC-PMT. The positioning equations were

$$X = \frac{X_+ - X_-}{X_+ + X_-} \quad \text{and} \quad Y = \frac{Y_+ - Y_-}{Y_+ + Y_-} \quad (1)$$

the standard Anger logic equations, where each dimension (X or Y) is normalized by its own total signal.

A fifth, variable resistor was also connected to each element and grounded. This potentiometer acts strictly to bleed charge to ground, allowing passive gain balancing of all 19 pixels in the imaging array. Simulations to optimize the resistive divider were performed using the Electronic Workbench™ (Interactive Image Technologies) package and com-

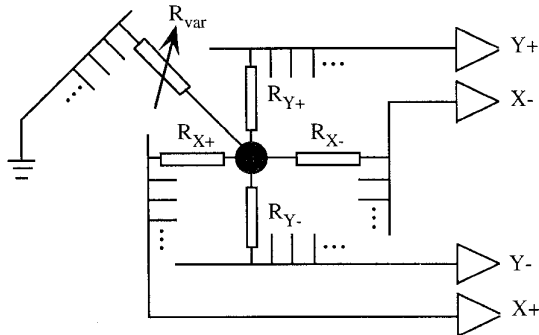


FIGURE 12. Schematic of the charge division network for a single pixel. Each pixel's charge is divided in proportion to the resistor value, based on the Cartesian location of the element in the hexagonal array. All resistors in a single direction are bused together and pre-amplified with 2 μ sec shaping time. A fifth bus through a potentiometer to ground acts as the gain balancing component.

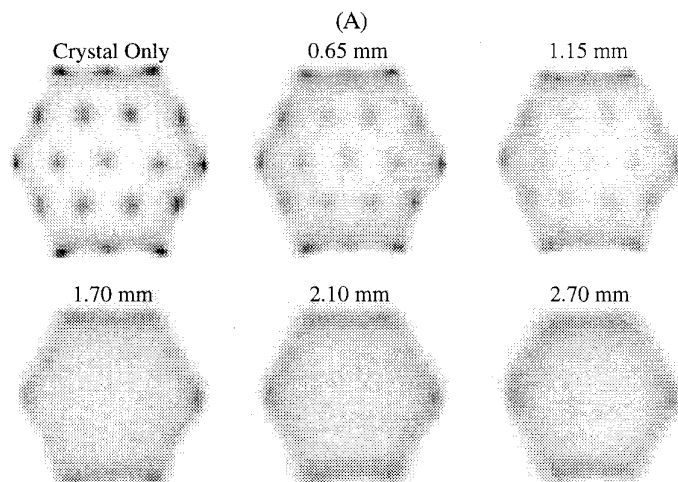


FIGURE 14. (A) Six images (64 x 64 pixels, 256 gray levels) of the flood field responses of the beta imaging device with $\text{CaF}_2(\text{Eu})$ coupled to DCPS optical fibers without or with various thickness PS light diffusers. (B) Differential uniformity measured for PMMA and PS light diffusers as a function of thickness. $\pm \sigma$ % is measured as the standard deviation from the mean pixel value in the CFOV.

pared to measured values with DC currents (Fig. 13). Note the excellent 2D linearity of the measured data with $\pm 5\%$ resistors employed for the positioning. The four resistors from each pixel element are bused together depending on their X_+ , X_- , or Y_+ , Y_- location, and the resultant divided charge from each element is fed to an i -V preamplifier (Maxim 410), with 2 μ sec shaping (feedback), and 50 Ω line driver (National Semiconductor LM6321). The resultant voltage signals were further amplified, shaped, discriminated and digitized with standard NIM and CAMAC electronics. Data acquisition control, analysis and image processing were performed on list mode data with a Macintosh IIfx platform using LabVIEW™ (National Instruments), and a VAX4000 system (Fig. 1).

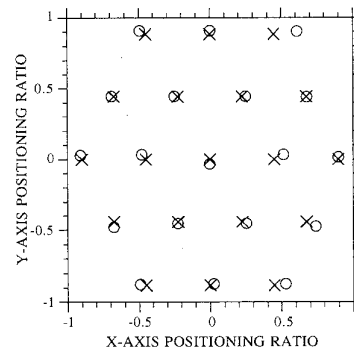
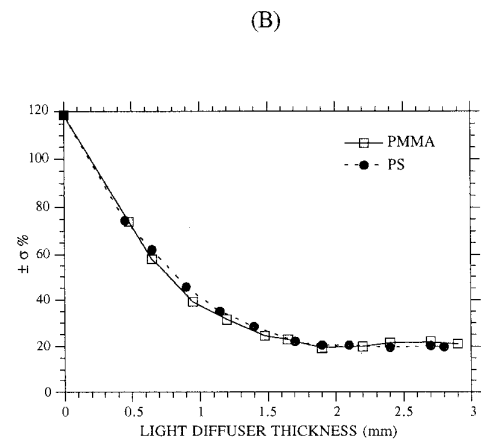


FIGURE 13. 2D linearity comparison of simulated positions (X) and measured positions (O) determined from Eqn. (1). The measured results were made with $\pm 5\%$ resistors.

V. IMAGING CHARACTERISTICS

A. Light Sharing & Uniformity

For the continuous imaging detector system described in this work, the thickness and transmission of the light diffuser are critical to the spatial and uniformity response of the imaging device. As the thickness of the light diffuser increases (Fig. 14A), the pseudo-discretized imaging device



becomes one that can image continuously between the 19 front-end fiber elements (cf. section II.B.). The flood field responses (images) of the PMMA and PS light diffusers were similar for a given thickness. All light diffusers were 1.25 cm ϕ and had roughened sides painted with black absorber (cf. section II.A.).

With a 1.7 mm thick PS light guide, the fiber “hot spots” just disappear in a gain balanced flood field image (Fig. 14A). Another effect seen in these flood field images is that the image dynamic range decreases with increasing light guide thickness. This result is not surprising since increasing light diffuser thickness corresponds to a decrease in solid angle from the scintillator to the optical fibers, especially at the edges of the imaging device. The edge effects in this device are common to light sharing gamma camera systems [27].

Moreover, as the light diffuser thickness increases, the uniformity ($\pm\sigma$ % is the standard deviation from the mean pixel value) in the center FOV (CFOV \approx 75% area in the center of the flood image) dramatically improves (Fig. 14B). Although the best uniformity was just $<20\%$, these measurements were made with ~ 36 cts/pixel in the image, which leads to 17% statistical error alone. When >150 cts/pixel were acquired with a 1.7 mm PS light guide, the uniformity improved to $\pm 15.6\%$ (with 8% statistical error alone).

The 1.7 mm thick PS light diffuser was chosen for all further experiments because it (1) had higher light output than a similar PMMA light diffuser (Fig. 4), (2) was the thickness at which the fiber “hot spots” disappeared (Fig. 14A), and (3) was the thickness at which the asymptotic minimum $\pm\sigma\%$ was reached (Fig. 14B). Thicker light diffusers also had poorer pulse height responses.

B. System Spatial Resolution

The system spatial resolution was measured with a ^{204}Tl source collimated through a 0.1 mm slit in a 1 cm thick black PMMA collimator directly in contact with the front surface of the imaging detector with white fiber holder. This line source was stepped in the X and Y dimensions in 1.0 mm increments. Profiles were drawn perpendicular to the resultant line images and fit with Gaussians.

Several thicknesses of PS light guides were utilized to see how the resolution degraded with increased light sharing (Fig. 15A). The surprising result obtained is, clearly, that the spatial resolution does not degrade with increased light sharing. Furthermore, for the PS thicknesses tested, there was an $\sim 20\%$ decrease in pulse height (Fig. 4) but no degradation in spatial resolution. One explanation for this effect is that with this optimized short fiber bundle (2 mm ϕ by 10 cm long DCPS), the light level is so large that a 20% variation has a very small statistical effect. For 2 m lengths of fiber where we expect factors of 4 lower light (Table 3), this same 20% variation is expected to become a much larger effect in positioning.

With the 1.7 mm thick PS light diffuser, the spatial resolution was also measured for the various fiber holders (Fig. 15B). The spatial resolution varied slightly from 0.58 mm \pm 0.071 mm to 0.50 mm \pm 0.038 mm in X, and from 0.67 mm \pm 0.066 mm to 0.55 mm \pm 0.065 mm in Y for the white and black holders, respectively. The small differences are likely due to the absorption of photons in the black holder that otherwise would have reflected off the white fiber support

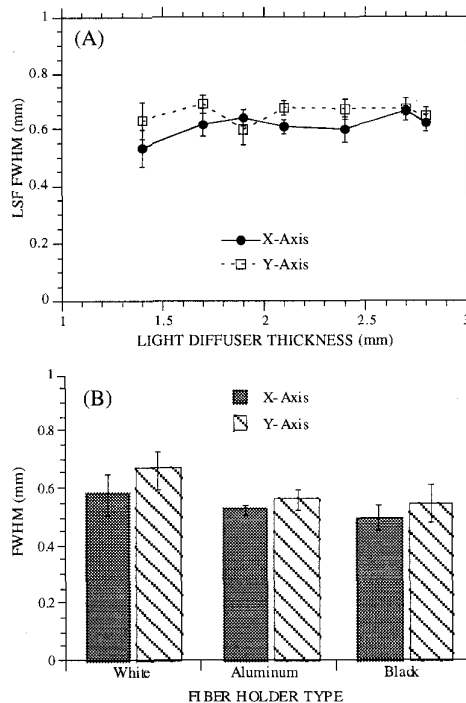


FIGURE 15. (A) System spatial resolution as a function of PS light diffuser thickness. Note that for the thicknesses indicated, there is an $\sim 20\%$ drop in pulse height with no significant effect on resolution. The white fiber holder was used with PS light diffusers. (B) Measured system spatial resolution with a 1.7 mm PS diffuser. There is an improvement in spatial resolution due to the absorptive properties of the fiber holders.

structure (see Fig. 8 and [31]). These reflected photons would in turn have been mispositioned. The spatial (image) resolution measurements with the different holders are consistent with improvements seen in the single fiber LTSF measurements and simulations.

Since beta distributions in tissues will be uncollimated (i.e. 2π distribution), we imaged <1 mm ϕ drops of ^{18}F and ^{68}Ga ($E_{\beta^+ \text{ max}} = 1.9$ MeV) in air and in a PMMA scattering medium in contact with the detector. The FWHM resolutions measured 1.10, 1.15 and 1.24, 2.14 mm for ^{18}F and ^{68}Ga , with and without the scattering media, respectively. These results indicate that beta straggling (energy dependent range) in tissues plays a larger role than penetration in the detector.

C. Preliminary Imaging Results

Using the 0.5 mm thick $\text{CaF}_2(\text{Eu})$ crystal coupled to the 1.7 mm PS light diffuser and white fiber holder with 10 cm long DCPS fibers, some preliminary images were made using ^{204}Tl . A 0.4 mm thick copper transmission mask was made with 0.5 mm ϕ holes spaced on 0.6 mm centers (Fig. 16A). Two images were collected, as the mask did not fit entirely into the FOV of the beta imaging probe, and digitally spliced together (Fig. 16B). Note the good separation of the horizontal and vertical lines, especially internal to the “#” and top of the letter ‘A’. The non-linearities, although minimal, can partially be compensated for by adjusting the gains of each MC-PMT pixel element. The high resolution is important for the device performance, so that partial volume effects due to

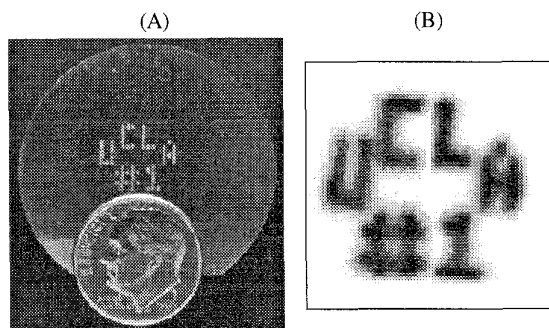


FIGURE 16. (A) Transmission phantom: 0.4 mm thick Cu plate with 0.5 mm ϕ holes spaced 0.6 mm apart horizontally and vertically. Dime is included for scale and is actual size in the photo. (B) Composite image (64 x 64 pixels, 256 gray levels, 220k events) made with ^{204}Tl through transmission phantom in the 10.8 mm FOV.

poorer resolution do not wash out small areas of increased activity. Image pixel resolution can be chosen depending on the resolution quality necessary for a given *in situ* situation.

VI. CONCLUSIONS

We are developing a beta sensitive, small area (1.2 cm²) imaging device intended for *in situ* use. The size of the device is small enough to fit into small surgical openings while large enough to produce images of clinical value.

The best scintillator was a 0.5 mm thick by 1.25 cm ϕ CaF₂(Eu) scintillator with a ground upper surface covered with a thin layer of Teflon tape and roughened absorbing sides [22]. Further studies are needed to determine the type of reflector for use in ambient surroundings. The optimum light diffuser using a white fiber holder was found to be a 1.7 mm thick by 1.25 cm ϕ PS disk with roughened and absorbing sides. The Kuraray DCPS fibers had the best transmission properties for the CaF₂(Eu) scintillator and, of the fibers tested, were also the easiest to work with. Although the highest pulse height was achieved with a white fiber holder surrounding the bundle of 19 hexagonally arranged fibers, the best spatial resolution (0.50 mm \pm 0.038 mm in X) was found with a black fiber holder which acted to absorb reflected, randomized events. Moreover, a 20% variation in pulse height, with 164% increase in PS light diffuser thickness had no significant effect on spatial resolution. This is thought to be due to the large pulse height seen for short lengths of fibers where cladding transmission plays a significant role in total light transmission. For the longer (2 m) more flexible fiber bundles, larger losses, as measured for a single bundle case, are anticipated with a corresponding resolution degradation.

The parallel PD readout is an important aspect of the signal division. The primary signal division is performed in the scintillator and front-end light diffuser. The light generated in the scintillator has spatial information in that the point of origination subtends a fixed solid angle to the front-end fiber optics. Once the light enters the fibers, all spatial information is lost within the 2 mm ϕ fiber due to the light propagation in a step-index, multi-mode optical fiber; i.e. light rays travel meridionally, axially, etc. If the PD receiving the signal from the fibers has large optical crosstalk, as from a continuous glass faceplate position-sensitive PMT, the light from these fibers (whose information is an intensity) can recombine in an

unfavorable way and either seriously blur or completely corrupt the recombined light signal intensities. The 64 channel Philips XP1722 FO windowed MC-PMT measures considerably smaller optical cross-talk (41% less) than its glass windowed counterpart and is thus considered well suited as a discretized PD package for this imaging application. With the large pixels (2.54 mm square) on the MC-PMT, this MC-PMT can measure the \sim 75 PEs that propagate through the fiber optic imaging chain.

The gain balancing, resistive charge division circuit, which mixes and recombines the electrical signals generated from the MC-PMT, works well with the measured signal levels. Further investigation of gain balancing methods is underway to improve both image uniformity and linearity. Linearity and image reconstruction methods utilizing MLE methods may also prove useful for optimal device performance.

Previous measurements on the device sensitivity indicate that with a low threshold on the ^{204}Tl beta spectrum, the device sensitivity is \sim 8400 cps/ μCi of radioactivity [20]. Further measurements to understand the device performance in the clinical setting will include: (1) ambient light shielding; (2) phantom testing with scatter media and realistic backgrounds to determine minimum detectable activities and image quality; (3) background correction techniques; (4) long term stability testing; and (5) animal models combined with relevant radiopharmaceuticals to determine *in situ* imaging ability. Along with the achieved high spatial resolution, the beta imaging intra-operative imaging probe is sensitive to small areas and amounts of radioactivity. These performance parameters will enable a surgeon to dynamically image and identify residual radiolabeled tumor deposits for subsequent removal.

VII. ACKNOWLEDGMENTS

The authors would like to thank Philips Photonics for lending the use of the XP1700 MC-PMTs, Dr. Simon Cherry, Dr. Keith Black, Ezzo Flyckt, Wayne Seemungal, and also Thomas Farquhar for helpful discussions, Drs. Jay Hauser and Yuri Bonushkin for help with the crosstalk measurements, Dr. Muzaffer Atac for providing sample fibers, Ken Meadors and Gerold Moffat for expert technical assistance, and Kuraray Int'l, Incom, Electro-Fiber Optics, Spectran, and Fiberguide for material samples. This work was funded in part by DOE contract DE-FC03-87-ER60615 and NCI grant R01-CA61037.

VIII. REFERENCES

- [1] Selected papers from the *Society of Nuclear Medicine Conference*, 12-15 June 1995, Minneapolis, MN, and in *J. Nuc. Med.* **36**(5), 1995. (1) T Hill, *et al.* Mapping of Melanoma Sentinel Lymph Node Using $^{99\text{m}}\text{Tc}$ Sulfur Colloid and the Neoprobe 1000 Intraoperative Detector. p.197P. (2) BAE Kapteijin, *et al.* Lymphoscintigraphy and Intraoperative Gamma Probe Detection of the First Draining Lymph Node in Clinically Localized Melanoma. p.222P. (3) R Essner, *et al.* Preoperative and Intraoperative Lymphatic Mapping Employing $^{99\text{m}}\text{Tc}$ Human Serum Albumin for Early Stage Melanoma. p.223P. (4) J Vansant, *et al.* Lymphoscintigraphy Defines a Surgical Approach to Patients with Clinical Stage I Melanoma. p.223P. (5) MP Bedigian, *et al.* Intraoperative Localization of SPECT Detected Parathyroid Adenomas and Assessment of Completeness of Tumor Excision Using a Hand-Held Radiation Detector Probe. p.228P.

- (6) A Mudun, *et al.* Reproducibility of Lymphoscintigraphy and Intraoperative Surgical Probe Use to Identify the Sentinel Node in Patients with Melanoma. p.263P.
- [2] B Selverstone, AK Solomon. 1948. Radioactive Isotopes in the Study of Intracranial Tumors. *Trans. Am. Neuro. Assoc.* **73**:115-119.
- [3] RA Lerch, HD Ambos, SR Bergmann, BE Sobel, MM Ter-Pogossian. 1982. Kinetics of Positron Emitters *In Vivo* Characterized with a Beta Probe. *Am. J. Physiol.* **242**(1):H62-H67.
- [4] H Reinhardt, D Stula, O Gratzl. 1985. Topographic Studies with ^{32}P Tumor Marker During Operations of Brain Tumors. *Eur. Surg. Res.* **17**(6):333-340.
- [5] F Daghighian, *et al.* 1994. Intra-operative Beta Probe: A Device for Detecting Tissue Labeled with Positron or Electron Emitting Isotopes During Surgery. *Med. Phys.* **21**(1):153-157.
- [6] RR Raylman, RL Wahl. 1994. A Fiber-Optically Coupled Positron-Sensitive Surgical Probe. *J. Nuc. Med.* **35**(5):909-913.
- [7] RR Raylman, SJ Fischer, RS Brown, SP Ethier, RL Wahl. 1995. ^{18}F -Fluorodeoxyglucose-Guided Breast Cancer Surgery with a Positron-Sensitive Probe: Validation in Preclinical Studies. *J. Nuc. Med.* **36**(10):1869-1874.
- [8] KL Swinth, JH Ewins. 1976. Biomedical Probe Using a Fiber-Optic Coupled Scintillator. *Med. Phys.* **3**(2):109-112.
- [9] HB Barber, JM Woolfenden, DJ Donahue, WS Nevin. 1980. Small Radiation Detectors for Bronchoscopic Tumor Localization. *IEEE Trans. Nucl. Sci.* **NS-27**(1): 496-502.
- [10] WC Harvey, JL Lancaster. 1980. Technical and Clinical Characteristics of a Surgical Biopsy Probe. *J. Nuc. Med.* **22**(2):184-186.
- [11] TS Hikernell, HB Barber, HH Barrett, JM Woolfenden. 1988. Dual-Detector Probe for Surgical Tumor Staging. *J. Nuc. Med.* **29**(6):1101-1106.
- [12] HB Barber, HH Barrett, JM Woolfenden, KJ Meyers, TS Hickernell. 1989. Comparison of *In Vivo* Scintillation Probes and Gamma Cameras for Detection of Small, Deep Tumors. *Phys. Med. Biol.* **34**(6):727-739.
- [13] JM Woolfenden, HB Barber. 1989. Radiation Detector Probes for Tumor Localization Using Tumor-Seeking Radioactive Tracers. *Am. J. Rad.* **153**(1):35-39 and references therein.
- [14] NE Hartsough, *et al.* 1989. Probes Containing Gamma Radiation Detectors for *In Vivo* Tumor Detection and Imaging. *Proc. SPIE: Catheter-Based Sensing and Imaging Technology.* **1068**:92-99.
- [15] EP Krenning, DJ Kwekkeboom, S Pauwels, LK Kvols, JC Reubi. 1995. Somatostatin Receptor Scintigraphy. *Nuclear Medicine Annual.* L.M. Freeman, Ed. pp.1-50.
- [16] K Kubota, *et al.* 1991. Tracer Feasibility for Monitoring Tumor Radiotherapy: A Quadruple Tracer Study with [^{18}F]-Fluorodeoxyglucose or [^{18}F]-Fluorodeoxyuridine, L-[Methyl- ^{14}C]Methionin, [$6\text{-}^3\text{H}$]Thymidine, and Gallium-67. *J. Nuc. Med.* **32**(11):2118-2123 and references therein.
- [17] BE Patt, JS Iwanczyk, MP Tornai, CS Levin, EJ Hoffman. 1995. Development of a Mercuric Iodide Detector Array for Medical Imaging Applications. *Nucl. Instr. Meth.* (In Press).
- [18] K Ljunggren, S-E Strand. 1990. Beta Camera for Static and Dynamic Imaging of Charged-Particle Emitting Radionuclides in Biologic Samples. *J. Nuc. Med.* **31**(12):2058-2063, and references therein.
- [19] LR MacDonald, *et al.* 1995. Investigation of the Physical Aspects of Beta Imaging Probes Using Scintillating Fibers and Visible Light Photon Counters. *IEEE Trans. Nucl. Sci.* **NS-42**(4):1351-1357 and references therein.
- [20] MP Tornai, *et al.* 1995. Development of a Small Area Beta Detecting Probe for Intra-Operative Tumor Imaging. *J. Nuc. Med.* **36**(5):109P.
- [21] LR MacDonald, *et al.* 1995. Small Area, Fiber Coupled Scintillation Camera for Imaging Beta-Ray Distributions Intra-Operatively. *Proc. SPIE: Photoelectronic Detectors, Cameras and Systems.* **2551**:92-101.
- [22] CS Levin, LR MacDonald, MP Tornai, EJ Hoffman, J Park. 1996. Optimizing Light Output from Thin Scintillators Used in Beta-Ray Camera for Surgical Use. *IEEE Trans. Nucl. Sci.* **NS-43**. In Press.
- [23] MP Tornai, EJ Hoffman, LR MacDonald, CS Levin. 1996. Characterization of Fluor Concentration and Geometry in Organic Scintillators for *In Situ* Beta Imaging. *IEEE Trans. Nucl. Sci.* **NS-43**. In Press.
- [24] HO Anger. 1958. Scintillation Camera. *Rev. Sci. Instr.* **29**(1):27-33.
- [25] RG Baker, JW Scrimger. 1967. An Investigation of the Parameters in Scintillation Camera Design. *Phys. Med. Biol.* **12**(1):51-63.
- [26] E Tanaka, T Hiramoto, N Nohara. 1970. Scintillation Cameras Based on New Position Arithmetics. *J. Nuc. Med.* **11**(9):542-547.
- [27] FD Rollo, Ed. 1977. *Nuclear Medicine Physics, Instrumentation, and Agents.* C.V. Mosby Company. St. Louis. Ch. 6.
- [28] HH Barrett, W Swindell, Eds. 1981. *Radiological Imaging: The Theory of Image Formation, Detection, and Processing.* Vol. 1. Academic Press. New York. Ch 5.
- [29] GF Knoll, TF Knoll, TM Henderson. 1988. Light Collection in Scintillating Detector Composites for Neutron Detection. *IEEE Trans. Nucl. Sci.* **NS-35**(1):872-875.
- [30] J Bradshaw, C Burnham, J Correia, WL Rogers, NH Clinthorne. 1985. Application of Monte-Carlo Methods to the Design of SPECT Detector Systems. *IEEE Trans. Nucl. Sci.* **NS-32**(1):753-757.
- [31] JS Karp, G Muehllhner. 1985. Performance of a Position-Sensitive Scintillation Detector. *Phys. Med. Biol.* **30**(7): 643-655.
- [32] JP O'Callaghan, R Stanek, LG Hyman. 1984. On Estimating the Photoelectron Yield and the Resultant Inefficiency of a Photomultiplier-Based Detector. *Nucl. Instr. Meth.* **225**(1): 153-163.
- [33] JT Remillard, MP Everson, WH Weber. 1992. Loss Mechanisms in Optical Light Pipes. *Appl. Opt.* **31**(34): 7232-7241.
- [34] B Baumbaugh, *et al.* 1994. Performance of Multiclad Scintillating and Clear Waveguide Fibers Read Out with Visible Light Photon Counters. *Nucl. Instr. Meth.* **A345**(2):271-278.
- [35] G Comby, R Meunier. 1988. Test of a New 64-Channel PMT for Imaging. *Nucl. Instr. Meth.* **A269**(1):246-260.
- [36] S Majewski, B Kross, R Wojcik, A Weisenberger, C Zorn. 1992. Studies of Position Sensitive Photomultipliers in Readout of Scintillating and Waveshifting Fibers. *Nucl. Instr. Meth.* **A323**(1-2):489-504.
- [37] Philips Photonics. 1993. *XPI700 Multi-Channel Photomultipliers Catalogue.*
- [38] P Cushman, S Hou. 1994. A Position Sensitive Detector for the G-2 Experiment Using Encircled Fibers. *Nucl. Instr. Meth.* **A339**(3):456-467.
- [39] MS Gerber, DW Miller, PA Schlosser, JW Steidley, AH Deutchman. 1977. Position Sensitive Gamma Ray Detectors Using Resistive Charge Division Readout. *IEEE Trans. Nucl. Sci.* **NS-24**(1):182-187.
- [40] S Siegel, RW Silverman, Y Shao, SR Cherry. 1996. Simple Charge Division Readouts for Imaging Scintillator Arrays Using a Multi-Channel PMT. *IEEE Trans. Nucl. Sci.* **NS-43**. In Press.